CT energy weighting in the presence of scatter and limited energy resolution

Taly Gilat Schmidt[a)]
Department of Biomedical Engineering, Marquette University, Milwaukee, Wisconsin 53201

(Received 29 June 2009; revised 8 January 2010; accepted for publication 9 January 2010; published 9 February 2010)

Purpose: Energy-resolved CT has the potential to improve the contrast-to-noise ratio (CNR) through optimal weighting of photons detected in energy bins. In general, optimal weighting gives higher weight to the lower energy photons that contain the most contrast information. However, low-energy photons are generally most corrupted by scatter and spectrum tailing, an effect caused by the limited energy resolution of the detector. This article first quantifies the effects of spectrum tailing on energy-resolved data, which may also be beneficial for material decomposition applications. Subsequently, the combined effects of energy weighting, spectrum tailing, and scatter are investigated through simulations.

Methods: The study first investigated the effects of spectrum tailing on the estimated attenuation coefficients of homogeneous slab objects. Next, the study compared the CNR and artifact performance of images simulated with varying levels of scatter and spectrum tailing effects, and reconstructed with energy integrating, photon-counting, and two optimal linear weighting methods: Projection-based and image-based weighting. Realistic detector energy-response functions were simulated based on a previously proposed model. The energy-response functions represent the probability that a photon incident on the detector at a particular energy will be detected at a different energy. Realistic scatter was simulated with Monte Carlo methods.

Results: Spectrum tailing resulted in a negative shift in the estimated attenuation coefficient of slab objects compared to an ideal detector. The magnitude of the shift varied with material composition, increased with material thickness, and decreased with photon energy. Spectrum tailing caused cupping artifacts and CT number inaccuracies in images reconstructed with optimal energy weighting, and did not impact images reconstructed with photon counting weighting. Spectrum tailing did not significantly impact the CNR in reconstructed images. Scatter reduced the CNR for all energy-weighting methods; however, the effect was greater for optimal energy weighting. For example, optimal energy weighting improved the CNR of iodine and water compared to energy-integrating weighting by a factor of $\sim$1.45 in the absence of scatter and by a factor of $\sim$1.1 in the presence of scatter (8.9° cone angle, SPR 0.5). Without scatter correction, the difference in CNR resulting from photon-counting and optimal energy weighting was negligible ($<$15%) for cone angles greater than 4.4° (SPR$>$0.3). Optimal weights combined with deterministic scatter correction provided a 1.3 and 1.1 improvement in CNR compared to energy-integrating and photon-counting weighting, respectively, for the 8.9° cone angle simulation. In the absence of spectrum tailing, image-based weighting demonstrated reduced cupping artifact compared to projection-based weighting; however, both weighting methods exhibited similar cupping artifacts when spectrum tailing was simulated. There were no statistically significant differences in the CNR resulting from projection and image-based weighting for any of the simulated conditions.

Conclusions: Optimal linear energy weighting introduces artifacts and CT number inaccuracies due to spectrum tailing. While optimal energy weighting has the potential to improve CNR compared to conventional weighting methods, the benefits are reduced as scatter increases. Efficient methods for reducing scatter and correcting spectrum tailing effects are required to obtain the highest benefit from optimal energy weighting.
[DOI: 10.1118/1.3301615]

Key words: energy-resolved CT, cone-beam CT, energy weighting, scatter, spectrum tailing

I. INTRODUCTION

Photon-counting detectors with energy-resolving capabilities enable optimal weighting of photons based on energy.[1–9] Conventional detectors, which integrate the detected signal, weight each photon proportionally to its energy. Detectors that count photons weight all photons equally. Both counting and integrating weighting schemes are suboptimal, as generally the low-energy photons carry the most contrast information.

The optimal energy weighting scheme for x-ray projection

imaging is to weight the data in each energy bin proportionally to the contrast-to-noise-variance ratio (CNVR) of the projection data in that bin.[1] This paper refers to the optimal weights for projection data as "projection-based" weights. A previous x-ray imaging study found that optimal energy weighting improved the contrast-to-noise ratio (CNR) in an x-ray projection by a factor of 1.4 compared to energy integrating in the absence of scatter.[7] In the presence of scatter, weights calculated without considering scatter were suboptimal and the CNR improvement was reduced to a factor of 1.1. The study proposed modifying the projection-based weights to account for scatter, which resulted in a 1.3 improvement in CNR compared to energy-integrating weighting.

Applying the optimal projection-based weights to CT requires weighting and combining the energy-bin data prior to log normalization. Previous works applied the optimal projection-based weights to CT and found that the CNR in the reconstructed images improved by factors of 1.1–1.6 depending on the task.[2,4–6] Because optimal weighting gives more weight to low-energy photons, beam hardening artifacts also increased.[3]

Beam hardening artifacts can be reduced if the energy-bin data are weighted and combined after log normalization.[7,9] Conceptually, this weighting scheme is equivalent to reconstructing separate images from each energy bin and then performing an optimal linear combination of the energy-bin images. The optimal weight for each energy-bin image is proportional to the CNVR in the image. This optimal "image-based" weighting scheme provided CNR improvement similar to optimal projection-based weights with reduced beam hardening artifacts.[9] A nonlinear combination of reconstructed energy-bin images was previously proposed to facilitate material decomposition in the image domain.[10] The decomposed basis images can then be used to reconstruct monoenergetic images with reduced beam hardening artifacts.

Previous studies of optimal energy weighting in CT did not consider realistic effects such as scatter and the contamination of low-energy bins from high-energy photons due to the nonideal detector response known as spectrum tailing. Both scatter and spectrum tailing are energy-dependent effects that more heavily impact low-energy bins. Since optimal energy weighting generally gives more weight to the low-energy photons, these effects are expected to be amplified by optimal energy weighting.

This paper investigates the combined effects of energy weighting, scatter, and spectrum tailing in CT imaging through simulations. In order to better understand the effects of spectrum tailing on the measured projection data, the paper first studies the effects of spectrum tailing on the estimated attenuation coefficients of homogeneous slab objects. While the focus of this paper is improved reconstruction of conventional CT images, the results of this study may be beneficial for material decomposition applications. The performance of energy weighting in the presence of spectrum tailing, scatter, and scatter correction is then investigated, with spectrum tailing and scatter considered both individually and in combination. A range of scattering conditions is simulated in order to determine the conditions at which the benefit of optimal energy weighting becomes negligible. For all simulations, both optimal image and projection-based linear weighting methods are investigated and compared.

II. METHODS AND MATERIALS

II.A. Theoretical considerations

Realistic energy-resolving detectors separate incoming photons into discrete energy bins.[2,11,12] For CT imaging, the energy-bin data are weighted and combined either before log normalization (projection-based weighting), as is the case for x-ray projection imaging, or after log normalization (image-based weighting). A brief review of optimal energy weighting is presented, followed by a derivation of the effects of spectrum tailing and scatter.

II.A.1. Projection-based weighting

The optimal linear weights for maximizing the CNR in an x-ray projection are proportional to the CNVR of the projection data in each energy bin.[1] In other words, the weights are proportional to the difference between the number of photons detected by a ray traveling through a background material and a ray traveling through the background material with an embedded contrast element, and inversely proportional to the noise in the projection measurement.

The CNVR of the projection data can be calculated empirically from the energy-bin data, although this measurement may be difficult to perform in practice. For projection data, the CNVR is independent of the number of incident photons and the size of the background object and therefore can be calculated analytically. In the absence of scatter, the optimal projection-based weights can be calculated for a specific task using a table of attenuation coefficients and the following equation:[4]

$$w_i = \frac{1 - e^{-[\mu_{c,i} - \mu_{b,i}]d}}{1 + e^{-[\mu_{c,i} - \mu_{b,i}]d}}, \tag{1}$$

where $\mu_{c,i}$ and $\mu_{b,i}$ are the average attenuation coefficients of the contrast element and background material, respectively, for the energy range of the ith bin, and d is the size of the contrast element. Approximate weights were proposed that do not require knowledge of the specific task.[4,6]

II.A.2. Image-based weighting

A different approach for optimal linear energy weighting in CT is to weight and combine the energy-bin data after log normalization in order to reduce beam hardening artifacts. In this case, the optimal weights w_i are proportional to the CNVR of the reconstructed energy-bin images, as described in Eq. (2),[9]

$$w_i \propto \frac{|\mu_{c,i} - \mu_{b,i}|}{\sigma_i^2} = \frac{C_i}{\sigma_i^2}. \quad (2)$$

The numerator in Eq. (2) reflects the contrast in the ith reconstructed energy-bin image and the denominator σ_i^2 reflects the noise variance.

The contrast in each energy-bin image can be calculated from tables of attenuation coefficients, approximated by analytical equations, or measured from regions of interest (ROIs) in the reconstructed energy-bin images. The energy-dependence of the noise, which in CT depends on the incident beam and the object, is measured either from the number of detected photons in each view or from ROIs in the reconstructed images.[9] Therefore, the noise is measured from the data, while the contrast is more easily determined from tables of attenuation coefficients or analytical approximations.

II.A.3. Spectrum tailing

Ideally, the detected energy of an incident photon is equal to the true photon energy. In reality, several effects in the detection process limit the ability of the detector to resolve the true photon energy.[5,13–17] One effect is the stochastic generation of electron-hole pairs in the detector, while a second effect is incomplete charge collection due to the trapping of holes. A third effect is charge sharing between neighboring pixels, which occurs when the energy deposited by an incoming photon is distributed between two detector pixels, resulting in each pixel measuring a lower energy photon. A fourth effect occurs when a K-fluorescence photon emitted during photoelectric absorption leaves the active pixel volume, causing the measured photon energy to be lower than the true energy. Pulse pile-up, an effect which is not considered in this paper, occurs when the pulses generated by multiple detected photons overlap, causing the photons to be detected as one high-energy photon. The effects of pulse-pile can be reduced by keeping the photon fluence below the count rate limitations of the detector.

When these detector nonidealities are present, the detector response has a Gaussian-shaped distribution around the true photon energy, a second Gaussian distribution with peak centered at the photon energy minus the K-fluorescence energy of the detector materials, and a nearly constant tail over the low energies due to charge sharing.[13] The specific shape of the detector response for a particular detector material depends on the energy of the incoming photon. Schlomka *et al.*[13] measured the energy response of a CdTe detector array at a synchrotron facility and developed a phenomenological model of the energy-dependent detector response. Figure 1 displays the detector response functions estimated by the Schlomka model for incident photon energies of 30, 45, 60, and 75 keV. The response curves are normalized to have an area of 1, thus the curves represent the probability that a detected photon at incident energy E' will be recorded as having energy E. By normalizing to 1, the assumption is made that all photons are detected. Nonideal detection efficiency can be modeled as a separate energy-dependent

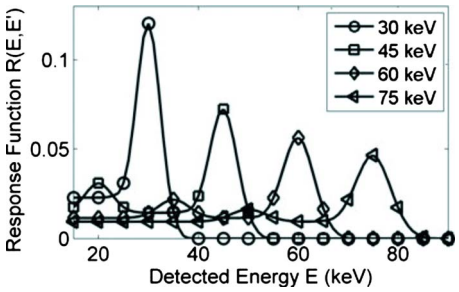

FIG. 1. Detector response functions modeled by Schlomka *et al.* (Ref. 13) for incident photons of 30, 45, 60, and 75 keV.

weighting factor.[16,17] Since the overall trend described in these curves is a low-energy tail of the detected photon energy (i.e., high-energy photons being detected as low-energy photons) this response is also referred to as spectrum tailing.[5,15]

In order to understand the effects of spectrum tailing on the measured signal, it is helpful to consider a polyenergetic pencil beam of photons traveling through a slab of linear attenuation coefficient $\mu(E)$ and thickness t. If the pencil beam has a spectrum of $N_o(E)$ incident on the slab, the spectrum detected behind the slab $\hat{N}(E)$ is

$$\hat{N}(E) = \int N_o(E')e^{(-\mu(E')t)}R(E,E')dE', \quad (3)$$

where $R(E,E')$ is the detector response function describing the probability of a photon at incident energy E' being detected at energy E (assuming that all photons incident on the detector are detected), as plotted in Fig. 1. The integral in Eq. (3) describes a shift-variant convolution over energy, with $R(E,E')$ representing the energy-dependent convolution kernel.

The estimated attenuation coefficient $\hat{\mu}(E)$ is

$$\hat{\mu}(E) = -\ln\left(\frac{\hat{N}(E)}{\int N_o(E')R(E,E')dE'} \cdot \frac{1}{t}\right), \quad (4)$$

where the denominator represents the detected raw-beam, which is also convolved by the nonideal detector response.

In photon-counting detection, all photons detected above a counting threshold are weighted equally and combined to form the final measurement. If all incoming photons are counted, the photon-counting measurement is unaffected by spectrum tailing. This is also evident in Eq. (3) because the detector response functions $R(E,E')$ are normalized to have an area of 1 for each incident photon energy E', and photon-counting detection essentially integrates $\hat{N}(E)$ over all detected energies E. In practice, some discrepancy will occur when two neighboring pixels count the same photon due to charge sharing and when a nonzero counting threshold is used to reject scatter and electronic noise.

The effects of spectrum tailing are more complex for energy-resolving detectors. The number of photons detected at energy E, $\hat{N}(E)$, can be decomposed into the number of photons incident on the detector at the energy E, $N(E)$, plus

an offset $\Delta N(E)$. The offset accounts for the number of photons erroneously detected at E and the number of photons with original energy E erroneously detected at other energies. Similarly, the number of raw-beam photons detected at energy E is equal to the number of photons incident on the detector $N_o(E)$ with an offset $\Delta N_o(E)$, reflecting the contributions to and from other energies. The true transmission fraction of the object is $T=N(E)/N_o(E)$, while the estimated transmission for the nonideal detector $\hat{T}(E)$ is

$$\hat{T}(E)=\frac{\hat{N}(E)}{\hat{N}_o(E)}=\frac{N(E)+\Delta N(E)}{N_o(E)+\Delta N_o(E)}. \tag{5}$$

If the estimated transmission is higher than the true transmission, the reconstructed object will appear less attenuating. This will occur under three conditions:

$$\Delta N(E),\Delta N_o(E)>0, \quad \frac{\Delta N(E)}{\Delta N_o(E)}>\frac{N(E)}{N_o(E)},$$

$$\Delta N(E),\Delta N_o(E)<0, \quad \frac{\Delta N(E)}{\Delta N_o(E)}<\frac{N(E)}{N_o(E)},$$

$$\Delta N(E)>0, \quad \Delta N_o(E)<0.$$

If the estimated transmission is lower than the true transmission, the reconstructed object will appear more attenuating. Since high-energy photons will be detected in lower energy bins, the noise in the reconstructed energy-bin images is expected to decrease for low energies and increase for high energies. As described in Eqs. (3) and (4), the magnitude of these effects depends on the incident spectrum, the object size and composition, as well as the binning and weighting of the energy data.

Since spectrum tailing is expected to affect both the contrast and noise variance in the energy-bin data, projection-based and image-based weights calculated assuming ideal conditions will no longer provide optimal CNR. In the case of image-based weighting, the weights calculated using Eq. (2) will be suboptimal because although the weights account for the noise in the data, the change in contrast due to spectrum tailing is not modeled. For a particular energy bin, the optimal weights can be calculated by measuring the contrast and noise variance in the reconstructed energy-bin images.

II.A.4. Scatter

The effects of scatter on the optimal projection-based and image-based weights can be described analytically. In the presence of scatter, projection-based weights calculated using Eq. (1) are suboptimal because the weights no longer reflect the CNVR in each energy bin. Scatter does not affect the difference between ray measurements through the background and contrast element, if the reasonable assumption is made that both rays measure the same average scatter signal. The noise variance in the projection increases with the detected scatter signal because more photons are detected. By neglecting the increased noise at low energies due to scatter, weights calculated using Eq. (1) give too much weight to low-energy photons.

The optimal projection-based weights in the presence of scatter, optimized to maximize CNR, can be expressed through a modification of Eq. (1) to reflect the CNVR, as described in Eq. (6).[7]

$$w_i \propto \frac{1-e^{-[\mu_{c,i}-\mu_{b,i}]d}}{1+e^{-[\mu_{c,i}-\mu_{b,i}]d}+2\cdot \mathrm{SPR}_i}, \tag{6}$$

where SPR_i is the ratio of scattered to primary photons detected in the ith energy bin. The modification in Eq. (6) reduces the weight of bins with high scatter-to-primary ratio (SPR).

To understand the effects of scatter on image-based weighting, the CNVR of the reconstructed images in the presence of scatter must be considered. As the SPR increases, the contrast in a CT image decreases according to Eq. (7).[18]

$$\hat{C}=(\mu_b-\mu_c)+\frac{1}{d}\ln\left(\frac{1+\mathrm{SPR}\cdot e^{[-(\mu_b-\mu_c)d]}}{1+\mathrm{SPR}}\right). \tag{7}$$

As derived in the Appendix, if $|(\mu_b-\mu_c)d|\ll 1$ and $|\mathrm{SPR}(\mu_b-\mu_c)d|\ll 1$, the contrast in the presence of scatter $\hat{C}$ is related to the contrast in the absence of scatter C by the following equation:

$$\hat{C}=C\left(\frac{1}{1+\mathrm{SPR}}\right). \tag{8}$$

As the number of scattered photons increases, the noise variance in a CT image decreases according to the approximate relationship[19]

$$\hat{\sigma}^2=\sigma^2\left(\frac{1}{1+\mathrm{SPR}}\right), \tag{9}$$

where σ^2 is the noise variance in the absence of scatter and $\hat{\sigma}^2$ is the variance in the presence of scatter.

The optimal image-based weights in the presence of scatter are proportional to the ratio of $\hat{C}$ to $\hat{\sigma}^2$, yielding the result that the optimal image-based weights are independent of scatter (i.e., weights optimized in the absence of scatter are optimal for all scatter conditions).

If the contrast is estimated from tables, which do not account for scatter, but the noise is measured from the data, which includes scatter, weights proportional to $C/\hat{\sigma}^2$ will be suboptimal. Because scatter reduces the noise variance, the suboptimal weights will give too much weight to the low-energy photons. Optimal weights can be calculated by adjusting the contrast estimate based on the scatter level.

$$w_i \propto \frac{|\mu_{c,i}-\mu_{b,i}|}{\hat{\sigma}_i^2(1+\mathrm{SPR}_i)}. \tag{10}$$

In summary, image-based and projection-based weights calculated without considering scatter will be suboptimal. Weights optimal in the presence of scatter can be calculated through measurements of contrast and noise in the data. If

TABLE I. Simulated system specifications.

Number of pixels (axial × transverse)	80 × 1600
Pixel size	0.25 × 0.25 mm^2
Source-to-isocenter distance	103.3 cm
Source-to-detector distance	165.3 cm
Number of views	500
Spectrum	120 kVp, 6 mm Al
m As	250
Cone angles	0.6°, 1.1°, 2,2°, 4.4°, 6.5°, 8.9°
Energy-bin ranges	[20–35], [35–45], [45–60], [60–90], [90–120] keV

such measurements are not feasible, the optimal weights can be calculated using Eq. (6) for projection-based weighting and Eq. (10) for image-based weighting, assuming an available estimate of the SPR in each energy bin.

If an estimate of the SPR in each energy bin is available, it is preferable to first correct for the deterministic effects of scatter by subtracting the estimated scatter signal. An ideal deterministic scatter correction will recover the contrast in the CT image, eliminate cupping artifacts due to scatter, but increase noise.[20] The net effect is an increase in CNR. In the case of scatter corrected images, the optimal weights are still proportional to the CNVR. For an ideal scatter correction that removes the mean scatter signal, the contrast can be determined from tables, while the noise is measured from the energy-bin data.

II.B. Simulation studies—Spectrum tailing and the estimated attenuation coefficient

In order to understand the combined effects of energy weighting and spectrum tailing, this paper first quantifies the effects of spectrum tailing on the estimated attenuation coefficient of homogeneous slab objects as discussed in Sec. II A 3.

The noiseless transmission of a polyenergetic pencil beam through homogeneous slabs of water and 0.75 mg/(cm^3) iodine was simulated. Slab thicknesses of 2–40 cm were simulated. The x-ray beam was simulated with a 120 kVp spectrum filtered with 6 mm of Al using the TASMIP software.[21] The spectrum was sampled from 20 to 120 keV at 1 keV intervals. The detector response functions derived by Schlomka *et al.*[13] were modeled discretely at 1 keV intervals with each response function normalized to have a sum of 1. The shift-variant convolution of the detected spectrum by the energy-dependent response functions was calculated discretely for the slab objects and used to estimate the attenuation coefficient $\hat{\mu}(E)$ as described in Eq. (11). The estimated attenuation coefficients were compared to the true attenuation coefficient at 1 keV intervals for each slab thickness and composition.

$$\hat{\mu}(E_k) = -\ln\left(\frac{\sum_{j=20}^{120} N_o(E_j')e^{(-\mu(E_j')t)}R(E_k,E_j')}{\sum_{j=20}^{120} N_o(E_j')R(E_k,E_j')}\right)\cdot\frac{1}{t}. \qquad (11)$$

II.C. Simulation studies—Energy weighting, spectrum tailing, and scatter

Simulation studies were performed to compare the CNR and artifact level of CT images reconstructed with energy-integrating, photon-counting, projection-based, and image-based weighting for varying scatter conditions and spectrum tailing effects. The effects of spectrum tailing were first studied assuming scatter-free conditions. Next the effects of scatter were studied assuming an ideal detector response. Finally, the combined effects of spectrum tailing, scatter, and energy weighting were investigated.

II.C.1. System configuration

The simulated CT system was based on a C-arm CT geometry whose scatter performance was previously studied.[18] The system specifications are listed in Table I. The simulated phantom was a 20-cm-diameter water cylinder of 20 cm length. The cylinder contained a 2-cm-diameter spherical contrast element of 7.5 mg/cm^3 iodine. The contrast element was located on the central slice of the phantom and 4 cm from the phantom center.

All simulations modeled a 120 kVp spectrum sampled at 1 keV intervals between 20 and 120 keV. The number of raw-beam photons incident on each detector pixel was calculated assuming the estimated raw-beam photon fluence of a typical 120 kVp, 250 m As scan.[22] For the simulations investigating spectrum tailing, the detector response functions of Schlomka *et al.*[13] were modeled as described in Sec. II B. The count rate and efficiency of the detector were assumed to be unlimited. To simulate a more realistic energy-resolving detector, all simulations binned the detected photons into five bins whose ranges are listed in Table I and whose performance was previously studied.[4] Because photon-counting detectors are expected to have negligible electronic noise, only noise due to photon-counting statistics was simulated.[23] All simulations were repeated ten times.

II.C.2. Spectrum tailing

The effects of spectrum tailing combined with energy weighting were first investigated assuming scatter-free conditions. Monoenergetic primary projections were analytically simulated at 20–120 keV in 1 keV increments. Because Poisson noise is caused by the stochastic processes of photon

generation and transmission, photon noise was simulated prior to convolution of the projection data with the energy-response functions. The simulation methods employed the following steps:

(1) Mean number of detected primary photons analytically calculated for monoenergetic x-rays;
(2) Poisson noise simulated based on mean number of detected photons;
(3) Shift-variant convolution across energy performed with energy-response functions $R(E,E')$; and
(4) Monoenergetic data binned into five discrete energy bins defined in Table I.

Overall, for each detector pixel along a ray path l, the number of photons detected in the ith energy bin $\hat{N}_i$ was calculated as

$$\hat{N}_i = \sum_{k=1}^{M_i} \sum_{j=20}^{120} \text{poiss}\left(N_o(E'_j)e^{-\int \mu(l,E'_j)dl}\right)R(E_k,E'_j), \quad (12)$$

where M_i represents the number of energies combined in the ith energy bin and poiss(λ) is a Poisson random variable with mean and variance equal to λ.

II.C.3. Scatter simulations

CT data with realistic scatter effects was generated through a previously described combination of Monte Carlo and analytical simulations.[24] A range of scattering conditions was simulated by varying the full cone angle from 0.6° to 8.9°. For each of the studied cone angles listed in Table I, Monte Carlo simulation software (GEANT 4) (Ref. 25) tracked the transport of 15×10^9 photons. Since the object is rotationally symmetric (except for the contrast element which has a negligible effect on scatter), a projection at one view angle was simulated to characterize the scatter at all view angles. The Monte Carlo simulations were performed on a 160 node high-performance computing cluster.

The simulated detector sorted the incoming photons into 1-keV-wide energy bins between 20 and 120 keV. In order to increase the number of detected counts in each pixel, and because the mean scatter signal contains primarily low frequencies, the detector in the Monte Carlo simulations was binned to 1×1 mm^2 pixels. For each detector pixel and energy bin, the number of detected primary and scattered photons was stored.

The mean scatter projection in each of the 1-keV-wide energy bins was determined by denoising the Monte Carlo results with the Richardson–Lucy fitting algorithm.[26] For each 1 keV energy bin, the mean scatter projection was linearly interpolated across the detector pixels to match the 0.25×0.25 mm^2 detector sampling of Table I and normalized to reflect the photon fluence simulated in the analytical simulations.

To summarize, CT data assuming an ideal detector response and realistic scatter was simulated with the following steps:

(1) Scatter simulated through Monte Carlo methods;

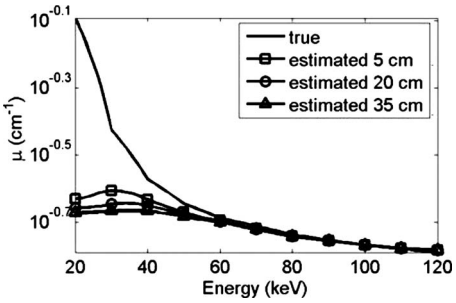

FIG. 2. The true linear attenuation coefficient of water compared to the attenuation coefficient estimated in the presence of spectrum tailing for varying material thicknesses.

(2) Mean scatter signal estimated by denoising Monte Carlo data;
(3) Mean number of detected primary photons analytically calculated for monoenergetic x rays;
(4) Mean number of detected primary and scatter photons combined for each energy;
(5) Poisson noise added based on the mean number of detected photons; and
(6) Monoenergetic data binned into five discrete energy bins defined in Table I.

For each detector pixel, the number of photons detected in the ith energy bin was

$$\hat{N}_i = \sum_{k=1}^{M_i} \text{poiss}\left(N_o(E'_k)e^{-\int \mu(l,E'_k)dl} + N_s(E'_k)\right), \quad (13)$$

where $N_s(E'_k)$ is the number of scattered photons incident on the detector pixel with energy E'_k.

To study the effects of scatter correction, projections were simulated after an ideal scatter correction that subtracted the mean scatter signal in each energy bin. The mean scatter signal, which in practice can only be estimated, was available from the Monte Carlo simulation results.

II.C.4. Combined spectrum tailing/scatter simulations

CT data was simulated including both the effects of scatter and spectrum tailing assuming an 8.9° cone angle. The overall simulation steps were

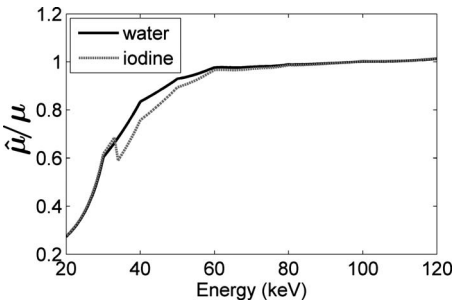

FIG. 3. The ratio of the estimated to true attenuation coefficients of water and iodine for a 20 cm slab thickness.

TABLE II. Applied energy weighting methods.

Weighting method	Weights	Number of energy bins	Width of energy bins
Integrating	E	101	1 keV
Counting	1	101	1 keV
PB	Equation (1)	5	Table I
IB	Equation (2)	5	Table I
IB_{opt}	$\propto C_{measured}/\sigma^2_{measured}$	5	Table I

(1) Scatter simulated through Monte Carlo methods;
(2) Mean scatter signal estimated by denoising Monte Carlo data;
(3) Mean number of detected primary photons analytically calculated for monoenergetic x rays;
(4) Mean primary and scatter signals combined for each energy;
(5) Poisson noise added based on the mean number of detected photons;
(6) Shift-variant convolution across energy performed with energy-response functions $R(E,E')$; and
(7) Monoenergetic data binned into five discrete energy bins defined in Table I.

For each detector pixel, the number of photons detected in the ith energy bin was

$$\hat{N}_i = \sum_{k=1}^{M_i} \sum_{j=20}^{120} \text{poiss}\left(N_o(E'_j)e^{-\int \mu(l,E'_j)dl} + N_s(E'_j)\right) R(E_k,E'_j). \tag{14}$$

II.C.5. Energy weighting

The following energy weighting methods were applied to the simulated data: Energy-integrating, photon-counting, projection-based weighting (PB) calculated using Eq. (1), image-based weighting (IB) calculated using Eq. (2), and image-based weights optimized for the true imaging conditions by measuring the contrast and noise in each reconstructed energy-bin image (IB_{opt}). The optimal image and projection-based weights for ideal conditions were calculated assuming the average attenuation coefficients of water and iodine in the energy range of each bin.[27]

For energy-integrating, photon-counting and optimal projection-based weighting, the energy-bin data were combined prior to log normalization, resulting in the line integral in the ith energy bin of a particular detector pixel equal to

$$\ell_{PB} = -\ln\left(\frac{\Sigma_{i=1}^{B} w_i \cdot \hat{N}_i}{\Sigma_{i=1}^{B} w_i \cdot \hat{N}_{o(i)}}\right), \tag{15}$$

where B is the number of energy bins.

For linear image-based weighting, the energy-bin data were combined after log normalization resulting in an estimated line integral of

$$\ell_{IB} = \sum_{i}^{B} -w_i \cdot \ln\left(\frac{\hat{N}_i}{\hat{N}_{o(i)}}\right). \tag{16}$$

Table II summarizes the applied weighting methods.

II.C.6. Image reconstruction and analysis

For all simulations, data from the central slice of the phantom were reconstructed with filtered backprojection onto an image with 440×440 pixels of size 0.5×0.5 mm^2. ROIs of 25×25 pixels were extracted from the contrast element and from the water background, both ROIs centered 4 cm from isocenter. The CNR was calculated from the mean and standard deviation in the ROIs, and averaged across the ten trials for each simulated case.

The cupping artifacts in the reconstructed images were quantified with a percent cupping metric.

$$\%\text{cupping} = 100 \cdot \frac{\mu_{edge} - \mu_{center}}{\mu_{edge}}. \tag{17}$$

Reconstructed images were converted to Hounsfield units (HU) using Eq. (18), which assumes an attenuation of water μ_{water}, equal to 0.2 cm^{-1}. Based on this conversion, the reconstructed HU value of water varied depending on the energy weighting scheme.

$$\text{HU} = 1000 \cdot \frac{\mu - \mu_{water}}{\mu_{water}}. \tag{18}$$

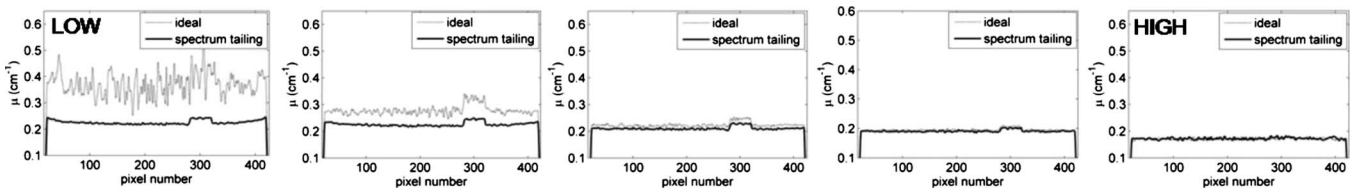

FIG. 4. Central horizontal profile through images reconstructed from the five energy bins simulated with ideal and spectrum tailing conditions.

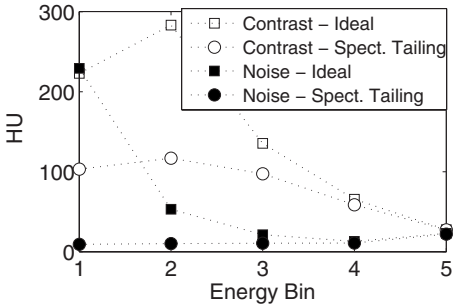

FIG. 5. Contrast and noise in energy-bin images simulated with ideal and spectrum tailing conditions.

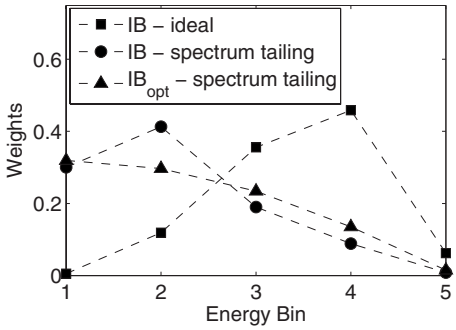

FIG. 6. Comparison of image-based weights calculated for ideal conditions (IB-ideal), spectrum tailing conditions using Eq. (2) (IB-spectrum tailing), and weights optimized for spectrum tailing by measuring both the contrast and noise in the energy-bin images (IB$_{opt}$-spectrum tailing).

Statistically significant differences between the CNR and cupping artifacts resulting from the different weighting methods or simulation conditions were determined using T-tests, with significance defined as $p<0.01$.

III. RESULTS

III.A. Spectrum tailing and the estimated attenuation coefficient

Figure 2 plots the true energy-dependent attenuation coefficient of water compared to attenuation coefficients estimated from data simulated with spectrum tailing for varying slab thicknesses, as described in Eq. (11). At low energies, spectrum tailing causes the estimated attenuation of water to be lower than the true value. The magnitude of the negative shift in attenuation coefficient increases with slab thickness. As energy increases, the discrepancy between the estimated and true attenuation coefficients decreases. Similar trends were observed for slabs of iodine. Figure 3 plots the ratio of the estimated to true attenuation coefficients of water and iodine for the 20 cm slab thickness. At 35–60 keV, the estimated attenuation coefficient of iodine is reduced by a larger factor than that of water, which indicates that spectrum tailing will also cause a reduction in contrast between the two materials. Overall, spectrum tailing causes an underestimation of the attenuation coefficient, and the error increases with material thickness and decreases with energy.

III.B. Energy weighting, spectrum tailing, and scatter

III.B.1. Spectrum tailing

In order to understand the effects of spectrum tailing on images reconstructed with different energy-weighting schemes, it is helpful to consider images reconstructed from each energy bin. Figure 4 compares the central horizontal profile through the reconstructed energy-bin images simulated with ideal and spectrum tailing conditions. For the low-energy bins, spectrum tailing causes a negative shift in the reconstructed values, with the lowest energy bin having the largest shift. The shifts are negligible for the higher energy bins. The two lowest energy bins also demonstrate increased cupping and reduced noise due to spectrum tailing.

Figure 5 plots the contrast and noise in the energy-bin images for ideal data and data simulated with spectrum tailing. This plot indicates that spectrum tailing decreases the contrast and noise at low energies. The image-based weights for each energy bin are plotted in Fig. 6. Weights optimized for ideal conditions (IB-ideal) are plotted. Also plotted are weights that use Eq. (2) for calculating the weights in the presence of spectrum tailing by estimating contrast from tables and noise from the data (IB-spectrum tailing), and weights optimized specifically for spectrum tailing by estimating contrast and noise from the data (IB$_{opt}$-spectrum tailing). In general, optimal image-based weights in the presence of spectrum tailing give more weight to the low energy bins compared to weights optimized for ideal conditions.

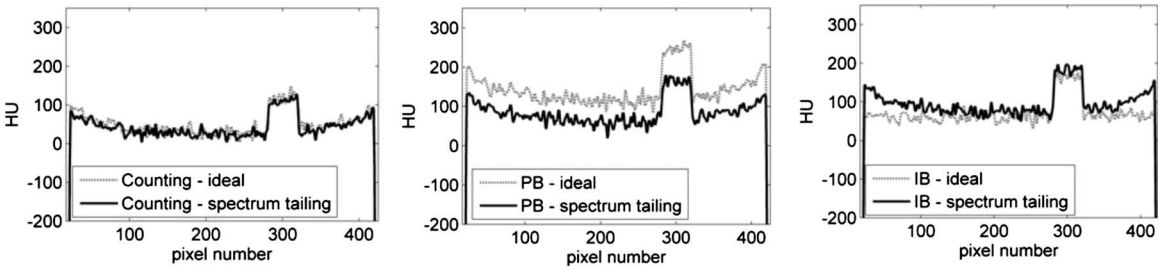

FIG. 7. Comparison of profiles of images reconstructed with photon-counting, projection-based, and image-based weights for ideal and spectrum tailing conditions.

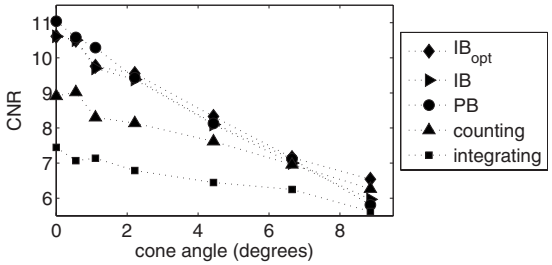

FIG. 8. CNR in images reconstructed with integrating, counting, optimal image, and projection-based weighting for a range of scatter conditions.

Since the optimal weights for spectrum tailing did not provide a statistically significant improvement in CNR or cupping artifacts compared to weights calculated with Eq. (2), all subsequent results assume image-based weights calculated with Eq. (2) (IB-spectrum tailing) unless otherwise specified.

Figure 7 compares profiles of images reconstructed with photon-counting, image-based weighting, and projection-based weighting for ideal and spectrum tailing conditions. As demonstrated in Fig. 7, spectrum tailing does not affect the photon-counting image, but introduces cupping and a positive shift in CT numbers in the image-based weighting image. Spectrum tailing causes a negative shift in the CT numbers for projection-based weighting.

III.B.2. Scatter with and without spectrum tailing

Figure 8 plots the CNR as a function of cone angle for the studied energy weighting methods without scatter correction and without spectrum tailing. As seen in Fig. 8, increasing scatter causes a reduction in CNR for all energy weighting methods; however, the effect is larger for optimal energy weighting. Therefore, the CNR benefit of optimal energy weighting decreases as the scatter increases. Figure 9 plots the CNR for integrating, counting, and image-based weighting after ideal deterministic scatter correction. Table III compares reconstructed CNR values for the five energy-weighting methods and the four simulation conditions. The listed values were averaged over the ten trials per simulation.

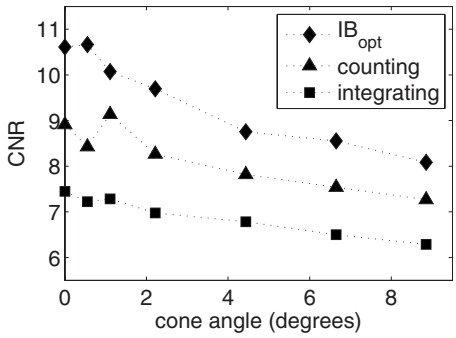

FIG. 9. CNR in images reconstructed with integrating, counting, and image-based weighting for a range of scatter conditions after ideal deterministic scatter correction.

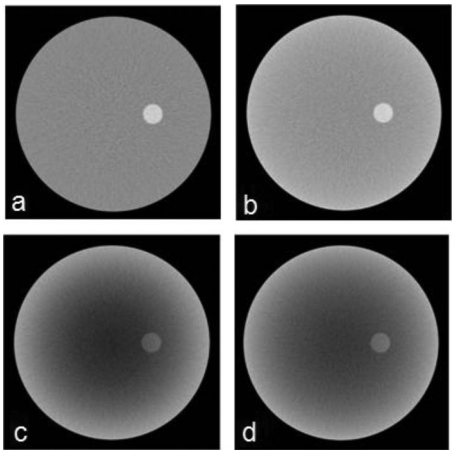

FIG. 10. Images reconstructed with image-based weighting under (a) ideal conditions, (b) spectrum tailing, (c) scatter (8.9°), and (d) combined scatter and spectrum tailing effects. All images are windowed to display −250 to 250 HU.

General trends can be summarized from Figs. 8 and 9 and Table III. In ideal scanning conditions, optimal energy weighting provides a 1.4 and 1.2 improvement in CNR compared to integrating and counting weighting, respectively. Spectrum tailing did not significantly affect the CNR. Scatter reduced the CNR in all cases, with the CNR reduced by 44% for optimal energy weighting compared to 25% and 30% for integrating and counting, respectively, for the 8.9° cone angle simulation. The CNR values resulting from projection and image-based weighting varied by less than 6% for all cases.

Figure 10 displays images reconstructed with image-based weighting for data simulated assuming ideal conditions, spectrum tailing, scatter with an 8.9° cone angle, and the combined effects of scatter and spectrum tailing. In all cases, the image-based weights were calculated using Eq. (2) (i.e., the weights were optimal only for the ideal case). All images are windowed to display CT numbers between −250 and 250 HU.

The profiles of images reconstructed from photon-counting, projection-based, and image-based weighting for ideal, scatter, and combined scatter/spectrum tailing conditions are plotted in Fig. 11, assuming an 8.9° cone angle. Table IV compares the percent cupping artifacts for the five weighting schemes and for the four simulation conditions. The listed values were averaged over the ten trials per simulation. For all three weighting methods, scatter increased the cupping artifact, with projection-based weighting demonstrating the overall highest cupping and image-based weighting demonstrating the largest increase in cupping due to scatter. The cupping artifacts were slightly reduced when spectrum tailing and scatter were both present compared to simulations modeling only scatter.

In ideal scanning conditions, image-based weighting provides negligible cupping artifacts (<1%); however, when spectrum tailing was present, photon counting, projection-based, and image-based reconstructions exhibited 6% cupping artifacts.

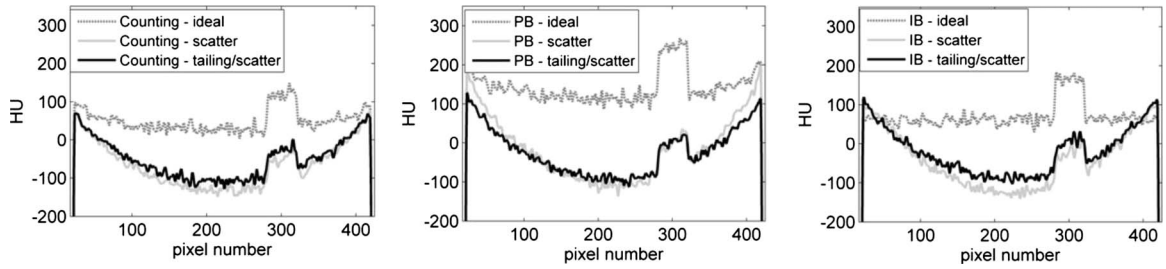

FIG. 11. Comparison of profiles of images reconstructed with photon-counting, projection-based, and image-based weights for ideal, scatter, and combined scatter/spectrum tailing conditions.

IV. DISCUSSION AND CONCLUSIONS

Spectrum tailing caused a negative shift in the estimated attenuation coefficients of slab objects at low energies as displayed in Fig. 2. This effect occurs because high-energy photons, which have higher transmission, are detected at lower energies leading to an overall apparent increase in transmission in the low-energy bins. This effect decreases with increasing energy because the overall contribution from higher energies decreases. The shift in attenuation coefficients becomes more negative with increased material thickness, causing cupping artifacts similar to beam hardening artifacts (Fig. 4).

As hypothesized in Sec. II A 3, spectrum tailing had a negligible effect on images reconstructed with photon-counting weighting. Images reconstructed with image-based weighting exhibited a positive shift in CT number and increased cupping due to spectrum tailing, while images reconstructed with projection-based weighting exhibited a negative shift in CT number. The negative shift in the projection-based weighted images is expected because spectrum tailing increases the apparent transmission fraction at low energies, and projection-based weighting gives the most weight to low-energy photons. Spectrum tailing did not increase the cupping artifact in images reconstructed with projection-based weighting (Table IV). One possible explanation of this result is that while spectrum tailing increases cupping, it also causes projection-based weighting to erroneously give high weight to high-energy photons thereby reducing beam hardening effects.[3] For image-based weighting, spectrum tailing causes low energy-bin images to exhibit a negative shift in HU value that increases with material thickness (Fig. 4). However, because spectrum tailing reduces the noise at low energies (Fig. 5), image-based weights give more weight to the low-energy bins under conditions of spectrum tailing compared to ideal conditions (see weights plotted in Fig. 6). Therefore, although the CT numbers are reduced for the low energy-bin images, the low energy bins are given more relative weight, resulting in the overall effect of a positive shift in CT number. Spectrum tailing did not significantly affect the reconstructed CNR for any of the studied weighting methods.

In general, image and projection-based energy weighting improved the CNR compared to energy-integrating and photon-counting weighting, but the benefit decreased as the scatter increased. In the absence of scatter, optimal energy weighting provided a 1.2 fold increase in CNR compared to photon counting. However, the CNR improvement was negligible ($<15\%$) for cone angles greater than 4.4°, assuming no scatter correction. For reference, the 4.4° and 8.9° cone angle simulations represent SPRs of 0.3 and 0.5, respectively (SPR calculated from the Monte Carlo results assuming energy-integrating weighting). Overall, the results of the scatter simulations indicate that scatter should be reduced as much as possible through acquisition and correction methods in order to obtain the maximum benefit from optimal energy weighting.

When both scatter and spectrum tailing effects were simulated, the reconstructed images exhibited slightly improved CNR ($\sim$1.1–1.3 fold) and reduced cupping ($\sim$0.8–1 fold) compared to simulations that modeled only scatter effects. This result suggests that spectrum tailing slightly mitigates the effects of scatter. While this conclusion requires additional study, one explanation is that spectrum tailing reduces the SPR in the low energy bins by contributing photons from higher energies that have lower SPR.

In the absence of spectrum tailing, image-based weighting demonstrated reduced cupping artifact compared to projection-based weighting. When spectrum tailing was simulated, both weighting methods exhibited similar cupping artifacts. There were no statistically significant differences in the CNR resulting from projection and image-based weighting for any of the simulated conditions.

TABLE III. Reconstructed CNR.

	Integrating	Counting	PB	IB	IB_{opt}
Ideal	7.5	8.9	11.0	10.6	10.6
Spectrum tailing	N/A	8.9	10.1	10.5	10.3
Scatter (8.9° cone angle)	5.6	6.3	5.8	6.0	6.5
Spectrum tailing and scatter	N/A	6.9	7.4	6.9	7.3

TABLE IV. Percent cupping artifact (Eq. (17)).

	Integrating	Counting	PB	IB	IB_{opt}
Ideal	4.1	5.9	7.3	0.19	0.19
Spectrum tailing	N/A	6.3	6.5	5.7	5.3
Scatter (8.9° cone angle)	14.9	17.9	24.1	19.1	16.0
Spectrum tailing and scatter	N/A	18.4	18.6	18.7	17.5

Image-based weights optimized for the specific imaging condition provided a negligible (~1.1 fold) improvement in CNR for the 8.9° cone angle simulation, but no statistically significant improvement in CNR or cupping when spectrum tailing was present. Therefore, image-based weights calculated using Eq. (2) will likely be reasonable for most applications.

In conclusion, optimal energy weighting introduces artifacts and CT number inaccuracies when the realistic detector effects of spectrum tailing are simulated. While optimal linear energy weighting has the potential to improve CNR compared to conventional weighting methods, the benefits are reduced as the scatter increases. Efficient methods for rejecting scatter and for correcting scatter and spectrum tailing effects are required to obtain the highest benefit from optimal energy weighting.

ACKNOWLEDGMENTS

Computer simulations were performed on the Marquette University High Performance Computing Cluster (NSF Grant No. CTS-0521602). The author would like to thank Lars E. Olson, PhD, and David Herzfeld (Marquette University) for help with the cluster and Chong Zhang (Marquette University) for assistance with the derivation in the Appendix.

APPENDIX: DERIVATION OF THE APPROXIMATE RELATIONSHIP BETWEEN CONTRAST AND SPR

The contrast in a CT image is defined as the difference between the reconstructed attenuation coefficients of two materials. The relationship between the reconstructed contrast $\hat{C}$, the SPR, and the contrast in the absence of scatter C is given in Eq. (A1) (Ref. 18)

$$\hat{C} = C + \frac{1}{d}\ln\left(\frac{(1+\mathrm{SPR}\cdot e^{-Cd})}{1+\mathrm{SPR}}\right),$$

$$C = \mu_b - \mu_c, \tag{A1}$$

where μ_b and μ_c are the true attenuation coefficients of a background material and contrast element, respectively, and d is the length of the contrast element.

Equation (A1) can be rewritten as

$$\hat{C} = C\left(1 + \frac{1}{Cd}[\ln(1+\mathrm{SPR}\cdot e^{-Cd}) - \ln(1+\mathrm{SPR})]\right). \tag{A2}$$

If $|Cd| \ll 1$, then Eq. (A2) is approximated by

$$\hat{C} \approx C\left(1 + \frac{1}{Cd}[\ln(1+\mathrm{SPR}-\mathrm{SPR}\cdot Cd) - \ln(1+\mathrm{SPR})]\right). \tag{A3}$$

Furthermore, if $\mathrm{SPR}\cdot|Cd| \ll 1$,

$$\ln(1+\mathrm{SPR}-\mathrm{SPR}\cdot Cd) \approx \ln(1+\mathrm{SPR}) - \mathrm{SPR}\cdot Cd\cdot(\ln x)'\big|_{x=1+\mathrm{SPR}}. \tag{A4}$$

Substituting Eq. (A4) into Eq. (A3) yields

$$\hat{C} \approx C\left(1 + \frac{1}{Cd}\left[\ln(1+\mathrm{SPR}) - \frac{\mathrm{SPR}\cdot Cd}{1+\mathrm{SPR}} - \ln(1+\mathrm{SPR})\right]\right) = C\left(\frac{1}{1+\mathrm{SPR}}\right). \tag{A5}$$

A previous study provided a different approximation for $\hat{C}$ that requires that $\mathrm{SPR} \ll 1$.[19] The approximation in Eq. (A5) is more accurate for larger SPR values as it requires only $\mathrm{SPR}\cdot|Cd| \ll 1$.

In the presented simulation studies, the highest SPR was 6 (lowest energy bin of the 8.9° cone angle simulation). In this case, the contrast between iodine and water predicted by Eq. (A1) was 0.0049, the contrast estimate by Eq. (A5) was 0.0051, and the measured contrast was 0.0043.

[a]Electronic mail: taly.gilat-schmidt@marquette.edu

[1]M. J. Tapiovaara and R. F. Wagner, "SNR and DQE analysis of broad spectrum x-ray imaging," Phys. Med. Biol. **30**(6), 519–529 (1985).
[2]P. M. Shikhaliev, "Tilted angle CZT detector for photon counting/energy weighting x-ray and CT imaging," Phys. Med. Biol. **51**(17), 4267–4287 (2006).
[3]P. M. Shikhaliev, "Beam hardening artefacts in computed tomography with photon counting, charge integrating and energy weighting detectors: A simulation study," Phys. Med. Biol. **50**(24), 5813–5827 (2005).
[4]P. M. Shikhaliev, "Computed tomography with energy-resolved detection: A feasibility study," Phys. Med. Biol. **53**(5), 1475–1495 (2008).
[5]P. M. Shikhaliev, "Energy-resolved computed tomography: First experimental results," Phys. Med. Biol. **53**(20), 5595–5613 (2008).
[6]J. Giersch, D. Niederlöhner, and G. Anton, "The influence of energy weighting on x-ray imaging quality," Nucl. Instrum. Methods Phys. Res. A **531**(1–2), 68–74 (2004).
[7]D. Niederlohner, J. Karg, J. Giersch, M. Firsching, and G. Anton, "Practical aspects of energy weighting in x-ray imaging," in Proceedings of the IEEE Nuclear Science Symposium Conference Record, October 2004, Vol. 5, pp. 3191–3194 (unpublished).
[8]D. Niederlohner, F. Nachtrab, T. Michel, and G. Anton, "Using the Medipix2 detector for photon counting computed tomography," in Proceedings of the IEEE Nuclear Science Symposium Conference Record, October 2005, Vol. 4, pp. 2327–2331 (unpublished).
[9]T. G. Schmidt, "Optimal 'image-based' weighting for energy-resolved CT," Med. Phys. **36**(7), 3018–3027 (2009).
[10]C. Maaß, M. Baer, and M. Kachelrieß, "Image-based dual energy CT

using optimized pre-correction functions: A practical new approach of material decomposition in image domain," Med. Phys. **36**(8), 3818–3829 (2009).
[11]S. S. Gleason, H. Sari-Sarraf, M. J. Paulus, D. K. Johnson, S. J. Norton, and M. A. Abidi, "Reconstruction of multi-energy x-ray computed tomography images of laboratory mice," IEEE Trans. Nucl. Sci. **46**, 1081–1086 (1999).
[12]V. Cajipe, R. Calderwood, M. Clajus, S. Hayakawa, R. Jayaraman, T. Tumer, B. Grattan, and O. Yossifor, "Multi-energy x-ray imaging with linear czt pixel arrays and integrated electronics," in Proceedings of the IEEE Nuclear Science Symposium Conference Record, October 2004, Vol. 7, pp. 4548–4551 (unpublished).
[13]J. P. Schlomka, E. Roessl, R. Dorscheid, S. Dill, G. Martens, T. Istel, C. Bäumer, C. Herrmann, R. Steadman, G. Zeitler, A. Livne, and R. Proksa, "Experimental feasibility of multi-energy photon-counting K-edge imaging in pre-clinical computed tomography," Phys. Med. Biol. **53**(15), 4031–4047 (2008).
[14]P. M. Shikhaliev, S. G. Fritz, and J. W. Chapman, "Photon counting multienergy x-ray imaging: Effect of the characteristic x rays on detector performance," Med. Phys. **36**(11), 5107–5119 (2009).
[15]S. Miyajima, K. Imagawa, and M. Matsumoto, "Cdznte detector in diagnostic x-ray spectroscopy," Med. Phys. **29**(7), 1421–1429 (2002).
[16]G. F. Knoll, *Radiation Detection and Measurement*, 3rd ed. (Wiley, New York, 2000).
[17]R. J. LeClair, Y. Wang, P. Zhao, M. Boileau, L. Wang, and F. Fleurot, "An analytic model for the response of a CZT detector in diagnostic energy dispersive x-ray spectroscopy," Med. Phys. **33**(5), 1329–1337 (2006).
[18]J. H. Siewerdsen and D. Jaffray, "Cone-beam computed tomography with a flat-panel imager: Magnitude and effects of x-ray scatter," Med. Phys. **28**(2), 220–231 (2001).
[19]M. Endo, S. Mori, T. Tsunoo, and H. Miyazaki, "Magnitude and effects of x-ray scatter in a 256-slice CT scanner," Med. Phys. **33**(9), 3359–3368 (2006).
[20]L. Zhu, J. Wang, and L. Xing, "Noise suppression in scatter correction for cone-beam CT," Med. Phys. **36**(3), 741–752 (2009).
[21]J. M. Boone and J. A. Seibert, "An accurate method for computer-generating tungsten anode x-ray spectra from 30 to 140 kV," Med. Phys. **24**(11), 1661–1670 (1997).
[22]J. A. Seibert, "X-ray imaging physics for nuclear medicine technologists. Part 1: Basic principles of x-ray production," J. Nucl. Med. Technol. **32**(3), 139–147 (2004).
[23]P. M. Shikhaliev, T. Xu, and S. Molloi, "Photon counting computed tomography: Concept and initial results," Med. Phys. **32**(2), 427–436 (2005).
[24]R. Bhagtani and T. G. Schmidt, "Simulated scatter performance of an inverse-geometry dedicated breast CT system," Med. Phys. **36**(3), 788–796 (2009).
[25]S. Agostinelli *et al.*, "G4—A simulation toolkit," Nucl. Instrum. Methods Phys. Res. A **506**(3), 250–303 (2003).
[26]A. P. Colijn and F. J. Beekman, "Accelerated simulation of cone beam x-ray scatter projections," IEEE Trans. Med. Imaging **23**(5), 584–590 (2004).
[27]J. H. Hubbell and S. M. Seltzer, "Tables of X-ray mass attenuation coefficients and mass energy-absorption coefficients 1 keV to 20 MeV for elements $Z=1$ to 92 and 48 additional substances of dosimetric interest," Report NISTIR5632, U.S. Department of Commerce, Gaithersburg, MD (1995).